Chapter 6

Phase-Locking and Coherent Beam Combining of Broadband Linearly Chirped Optical Waves

6.1 Introduction

Optical phase-locking has found various applications in the fields of optical communication links [52, 78–81], clock generation and transmission [82, 83], synchronization and recovery [84, 85], coherence cloning [7], coherent beam combining (CBC) and optical phased arrays [8, 86–91], and optical frequency standards [92, 93], to name a few. In these applications, electronic feedback is used to precisely synchronize the phases of two optical waves. With a few notable exceptions [34, 94], prior demonstrations of phase-locking and synchronization have been performed using nominally monochromatic optical waves. In this chapter we describe our work on the phase-locking of optical waves whose frequencies are swept rapidly with time and over large chirp extents. The phase-locking of optical waves with arbitrary frequency chirps is a difficult problem in general. However, precisely linear chirps, such as the ones generated by the optoelectronic SFL (see chapter 3) can be phase-locked with very high efficiency using a frequency shifter. The main application of this result is the simultaneous stimulated Brillouin scattering (SBS) suppression and coherent combining of high-power fiber amplifiers. Other potential applications include electronic beam steering for lidar and 3-D imaging systems.

We begin our discussion by reviewing CBC approaches to the generation of high-power continuous-wave optical beams. We proceed to describe the basic principle behind phase-locking of linearly chirped optical waves, and present theoretical analyses of chirped-wave phase-locking in homodyne and heterodyne configurations. We demonstrate heterodyne phase-locking of chirped optical waves and implement a passive-fiber CBC system [10, 11]. We conclude with a description of our recent CBC experiment with two erbium-doped fiber amplifier (EDFA) channels [12]. The work described in this chapter was performed in collaboration with Jeffrey O. White's group at the United States Army Research Laboratory.

6.2 Coherent Beam Combining

The output power of optical fiber amplifiers is usually limited by SBS. Advances in the design of the geometry and doping profiles of active fiber have enabled increases in the SBS threshold power [95–97]. Further increases in the SBS threshold of a single amplifier can be obtained by broadening the linewidth of the seed laser through phase or frequency modulation [32,33]. A separate approach to achieving high optical powers is the coherent beam combining of the outputs of multiple laser or amplifier elements [8, 86–90].

The efficiency of a CBC scheme depends on the matching of the relative amplitudes, phases, polarizations and pointing directions of the multiple emitters in the array [86, 98, 99]. Phase synchronization of the array elements is a particularly difficult challenge, which in the past has been addressed with various approaches, including evanescent wave and leaky wave coupling of emitters [100, 101], common resonator arrays [102, 103], and phase-locking through optoelectronic feedback [8, 90]. In optoelectronic feedback systems, the phase error between the combined beams is measured and fed back to a phase actuator, such as an electro-optic phase modulator [87], acousto-optic frequency shifter [90], or a fiber stretcher [34, 89].

Kilowatt-level systems have been demonstrated [33] and rely on the simultaneous suppression of SBS in high-power fiber amplifiers and the CBC of multiple amplifier

channels. The path-length mismatch between array elements in an amplifier CBC system has to be much smaller than the seed coherence length, in order to prevent de-phasing due to incoherence. The traditional approach to SBS suppression relies on a broadening of the seed linewidth, and therefore a reduction of its coherence length. As a result, SBS suppression in high-power fiber amplifier CBC systems requires precise channel path-length matching. Recently, Goodno et al. [33] have demonstrated the phase-locking of a 1.4 kW fiber amplifier. This power level was achieved by increasing the SBS threshold using a modulated seed source with a linewidth of ~ 21 GHz. Efficient power combining was only possible with precise path-length matching of active fibers to sub-mm accuracy. Further increases in the power output of a single amplifier will require even broader seed linewidths, and path-length matching to within $\sim 10s$ of μm will be necessary. Weiss et al. [34] have recently demonstrated that coherent combining can still be achieved using a novel feedback loop that senses the path-length mismatch and corrects it using a fiber stretcher.

In this chapter we explore an architecture capable of SBS suppression and coherent beam combining without stringent mechanical path-length matching requirements [10–12]. Our approach is to use a rapidly chirped ($> 10^{14}$ Hz/s) swept-frequency laser (SFL) seed to reduce the effective length over which SBS occurs [35, 36]. The advantage of this approach is that path-length matching requirements are relaxed due to the long coherence length (several meters) of semiconductor laser based SFLs. In the following section we describe the basic principle of phase-locking of linearly chirped optical waves using acousto-optic frequency shifters (AOFSs) to compensate for static and dynamic optical path-length differences. We proceed with an analysis of homodyne and heterodyne optical phase-locked loop (OPLL) configurations, and present results of proof-of-concept experiments that demonstrate phase-locking, coherent combining, and electronic phase control in chirped-wave passive-fiber systems.
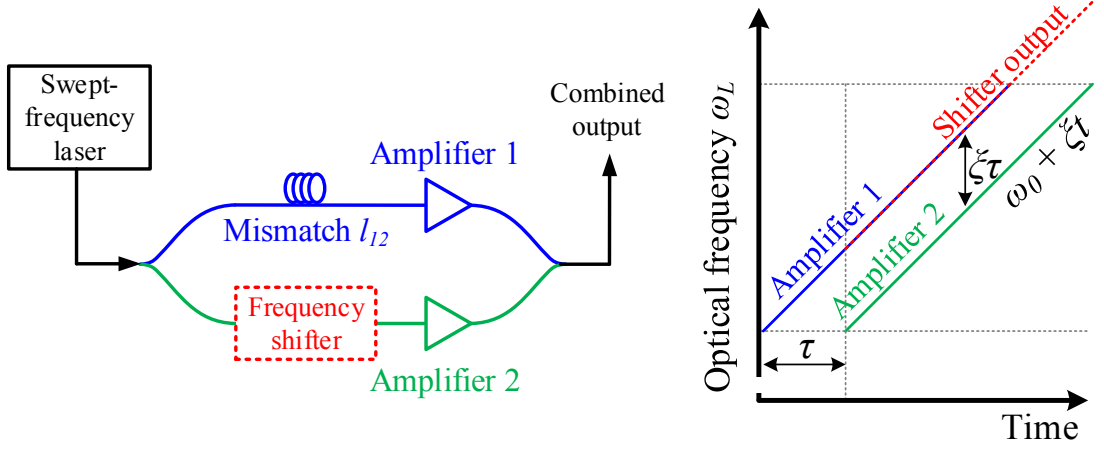
Figure 6.1: Intuitive description of chirped-seed amplifier coherent beam combining. A path-length mismatch between amplifier arms results in a frequency difference at the combining point, and can therefore be compensated using a frequency shifter placed before amplifier 2.

6.3 Phase-Locking of Chirped Optical Waves

The basic concept of phase-locking multiple chirped-seed amplifiers (CSAs) in a master oscillator power amplifier (MOPA) configuration is depicted in figure 6.1 [10, 11]. A SFL is used to generate a linear chirp, with an instantaneous optical frequency given by

$$\omega_L(t) = \omega_{L,0} + \xi t, \ \ 0 \leq t \leq T, \tag{6.1}$$

where $\omega_{L,0}$ is the initial optical frequency, ξ is the sweep rate, and T is the sweep time. The SFL is split into multiple amplifier seeds which then undergo amplification and recombination to form a high-power beam. A difference in the lengths of the fiber amplifiers 1 and 2 result in a frequency difference $\xi l_{12}/c$ at the locking point, where l_{12} is the path-length mismatch and c is the speed of light. An acousto-optic frequency shifter (AOFS) is placed in one of the arms to correct this frequency difference. For a linear chirp of $\frac{\xi}{2\pi} = 10^{15}$ Hz/s and a path-length mismatch of 10 cm in fiber, the required frequency shift is 500 kHz, which is well within the dynamic range of AOFSs. An optical phase-locked loop is formed by recording an interference signal between the two arms on a photodetector and feeding it back to the AOFS, as shown in figure 6.2 and figure 6.4. In lock, the AOFS synchronizes the optical phases and corrects

the fixed path-length mismatches as well as the dynamic length fluctuations arising from vibrations and temperature drift. The loop bandwidth determines the fastest fluctuation frequency that is suppressed, and previous work using AOFSs and single-frequency seeds has shown that sufficient bandwidths can be achieved for efficient combining of fiber amplifier outputs [90].

SBS suppression in high-power amplifiers scales with the chirp rate [35,36]. Therefore, we limit our attention to SFLs with perfectly linear chirps, in order to ensure that uniform SBS suppression is obtained throughout the duration of the frequency sweep. Moreover, a linear chirp enables path-length mismatches to be corrected by a constant frequency shift, as described above. Deviations from chirp linearity are corrected using a feedback loop, as long as these deviations are small and at frequencies within the loop bandwidth. It is therefore desirable that the chirp be close to perfectly linear, particularly at high chirp rates ξ, in order to relax the requirements on the frequency tuning range of the AOFS and the bandwidth of the feedback loop. We note that it should be possible to further extend the phase-locking approach to other sweep profiles, by using a time-varying frequency shift to compensate for the time-varying slope of the optical frequency chirp, e.g., using the iterative algorithm of section 3.2.3 to pre-distort the AOFS bias signal.

6.3.1   Homodyne Phase-Locking

We first consider the homodyne phase-locking configuration shown in figure 6.2. The output of an optoelectronic SFL is split into two arms using a fiber splitter. The goal of the experiment is to phase-lock the outputs of the two arms by feeding back the error signal generated using a 2×2 fiber coupler and a balanced detector. The bias frequencies and phase shifts of the two AOFSs are denoted by ω_1, ω_2 and ϕ_1, ϕ_2. The differential delay between the first and second arms is denoted by τ_{12}. We also introduce a common delay τ_d to model the long fiber length inside an optical amplifier. The feedback loop is very similar to a typical phase-locked loop [51], and can be analyzed accordingly. We define the DC loop gain K_{DC} as the product of the
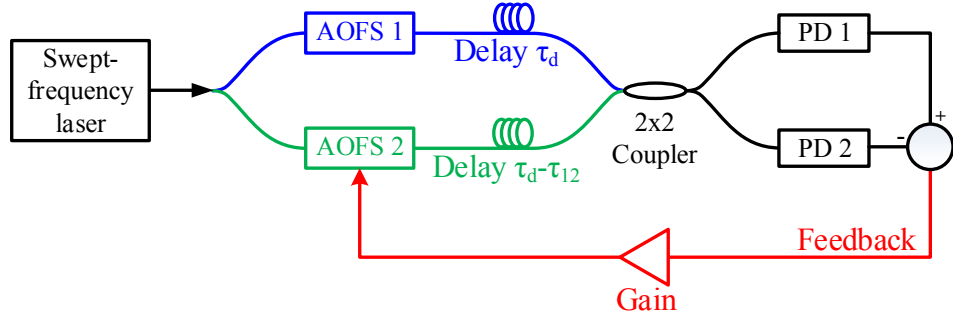
Figure 6.2: Passive-fiber chirped-wave optical phase-locked loop in the homodyne configuration. PD: Photodetector
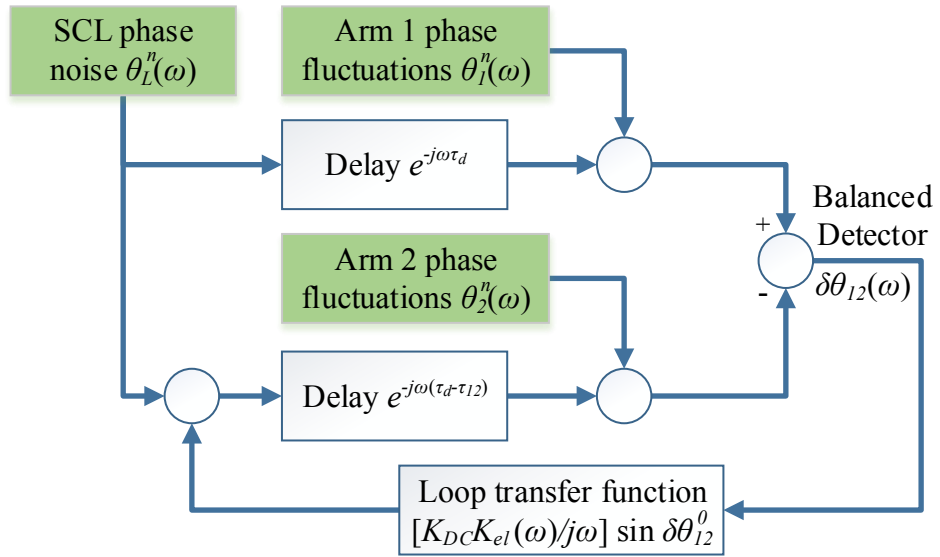

Figure 6.3: Small-signal frequency-domain model of the homodyne chirped-wave optical phase-locked loop. The model is used to study the effect noise and fluctuations (green blocks) on the loop output variable $\delta\theta_{12}(\omega)$.

optical power in each arm (units: W), and the gains of the balanced detector (V/W), loop amplifier (V/V), and frequency shifter (rad/s/V). Let the SFL optical frequency be given by equation (6.1), and let us denote the optical phases of the two arms at the coupler by $\theta_1(t)$ and $\theta_2(t)$. The optical phase difference between the two arms is given by

$$
\begin{aligned}
\theta_{12}(t) &\equiv \theta_1(t) - \theta_2(t) \\
&= (\omega_{L,0} + \omega_1)(t - \tau_d) + \frac{\xi}{2}(t - \tau_d)^2 + \phi_1 - (\omega_{L,0} + \omega_2)(t + \tau_{12} - \tau_d) \\
&\quad - \frac{\xi}{2}(t + \tau_{12} - \tau_d)^2 - \phi_2 - \int_0^{t+\tau_{12}-\tau_d} K_{DC}\cos\theta_{12}(u)\,du = \\
&= \Delta\omega_{fr}(t - \tau_d) - (\omega_2 + \omega_{L,0})\tau_{12} - \frac{\xi\tau_{12}^2}{2} + \phi_{12} - \int_0^{t+\tau_{12}-\tau_d} K_{DC}\cos\theta_{12}(u)\,du,
\end{aligned}
$$

(6.2)

where $\Delta\omega_{fr} \equiv \omega_1 - \omega_2 - \xi\tau_{12}$ is the free-running frequency difference between the two arms, and $\phi_{12} \equiv \phi_1 - \phi_2$. The final term in equation (6.2) represents the phase shift due to the feedback to the AOFS, which is the integral of the frequency shift. The steady-state solution θ_{12}^0, obtained by setting the time derivative of $\theta_{12}(t)$ to 0, is given by

$$
\theta_{12}^0 = \cos^{-1}\left(\frac{\Delta\omega_{fr}}{K_{DC}}\right).
$$

(6.3)

We use this result to rewrite equation (6.2),

$$
\theta_{12}(t) = \Delta\omega_{fr}(t + \tau_{12} - \tau_d) + \theta_{12}^0 - \int_0^{t+\tau_{12}-\tau_d} K_{DC}\cos\theta_{12}(u)\,du.
$$

(6.4)

In lock, the optical phases of the two arms differ by θ_{12}^0, and there is no frequency difference.

Next, we linearize the loop about its steady-state solution in order to study dynamic behavior and the effect of fluctuations. We denote the phase noise and residual nonlinearity of the SFL by $\theta_L^n(t)$, and the phase noise introduced in the two arms by $\theta_1^n(t)$ and $\theta_2^n(t)$, which include noise contributions from the AOFSs and fluctuations in the optical path lengths. We introduce $\delta\theta_{12}(t)$, the small-signal fluctuation of $\theta_{12}(t)$

about the steady state, so that

$$\theta_{12}(t) = \theta_{12}^0 + \delta\theta_{12}(t). \tag{6.5}$$

We plug equation (6.5) into equation (6.4), and expand about the steady-state point (equation (6.3)). Solving for $\delta\theta_{12}(t)$, we arrive at

$$\delta\theta_{12}(t) = \theta_{12}^n(t) + \theta_L^n(t - \tau_d) - \theta_L^n(t + \tau_{12} - \tau_d) + K_{DC}\sin\theta_{12}^0 \int_0^{t + \tau_{12} - \tau_d} \delta\theta_{12}(u)du, \tag{6.6}$$

where $\theta_{12}^n(t) \equiv \theta_1^n(t) - \theta_2^n(t)$. Taking the Fourier transform of both sides of equation (6.6), we arrive at a frequency-domain description of the small-signal fluctuations,

$$\begin{aligned} \delta\theta_{12}(\omega) = \theta_{12}^n(\omega) + \theta_L^n(\omega)\left[e^{-j\omega\tau_d} - e^{-j\omega(\tau_d - \tau_{12})}\right] \\ + \frac{K_{DC}K_{el}(\omega)\sin\theta_{12}^0}{j\omega}e^{-j\omega(\tau_d - \tau_{12})}\delta\theta_{12}(\omega), \end{aligned} \tag{6.7}$$

where $K_{el}(\omega)$ is the frequency-dependent gain of the loop electronics. This frequency-domain model is shown schematically in figure 6.3. The solution of equation (6.7) is given by

$$\delta\theta_{12}(\omega) = \frac{\theta_{12}^n(\omega)}{1 + K(\omega)} + \frac{\theta_L(\omega)\left[e^{-j\omega\tau_d} - e^{-j\omega(\tau_d - \tau_{12})}\right]}{1 + K(\omega)}, \tag{6.8}$$

where

$$\begin{aligned} K(\omega) &\equiv -\frac{K_{DC}K_{el}(\omega)\sin\theta_{12}^0}{j\omega}e^{-j\omega(\tau_d - \tau_{12})} \\ &= \frac{K_{DC}K_{el}(\omega)\sqrt{1 - \left(\frac{\Delta\omega_{fr}}{K_{DC}}\right)^2}}{j\omega}e^{-j\omega(\tau_d - \tau_{12})} \end{aligned} \tag{6.9}$$

is the total frequency-dependent feedback gain, and we picked the negative root in calculating $\sin\theta_{12}^0$ in order to achieve negative feedback.

In our experiments, loop bandwidths have been limited to the sub-MHz range by the AOFS frequency modulation response, and we therefore restrict our attention to the Fourier frequency range below ~ 10 MHz. Typical values of τ_{12} are in the ns

range, so $\omega\tau_{12} \lesssim 10^{-2}$, and we can expand equation (6.8) and equation (6.9) near $\omega\tau_{12} = 0$, yielding

$$\delta\theta_{12}(\omega) = \frac{\theta_{12}^n(\omega)}{1 + K(\omega)} - j\omega\tau_{12}\frac{\theta_L(\omega)e^{-j\omega\tau_d}}{1 + K(\omega)}, \text{ and} \qquad (6.10)$$

$$K(\omega) = \frac{K_{DC}K_{el}(\omega)\sqrt{1 - \left(\frac{\Delta\omega_{fr}}{K_{DC}}\right)^2}}{j\omega}e^{-j\omega\tau_d}. \qquad (6.11)$$

According to equation (6.10), phase fluctuations in the fiber are reduced by a factor $1 + K(\omega)$ in the locked state. For frequencies within the loop bandwidth, $K(\omega) \gg 1$, and significant noise suppression is obtained. The second term describes the effect of the SFL phase noise and residual chirp nonlinearity. The system behaves like a frequency discriminator with gain τ_{12}, and the feedback again suppresses the measured frequency noise by the factor $1 + K(\omega)$. It is clear that a small differential delay τ_{12} and an SFL with a highly linear chirp and low phase noise minimize the phase error in the loop.

The homodyne phase-locking approach described above has a few shortcomings.

1. The value of the steady-state phase θ_{12}^0 can only be adjusted (within the range $[0, \pi]$) by varying the bias frequency shifts ω_1 and ω_2; this is not optimal since it adversely impacts loop gain and therefore performance.

2. The desired operating point for in-phase beam combining is $\theta_{12}^0 \approx 0$; however, according to equation (6.9), the loop gain contains the factor $\sin\theta_{12}^0$, and the loop therefore loses lock as this operating point is approached. It is desirable that the loop be locked at quadrature $\theta_{12}^0 = \pi/2$, maximizing the gain.

3. Finally, it is not straightforward to scale this approach to multiple phase-locked arms.

These problems are all addressed by adopting a heterodyne phase-locking architecture, as described in the next section.
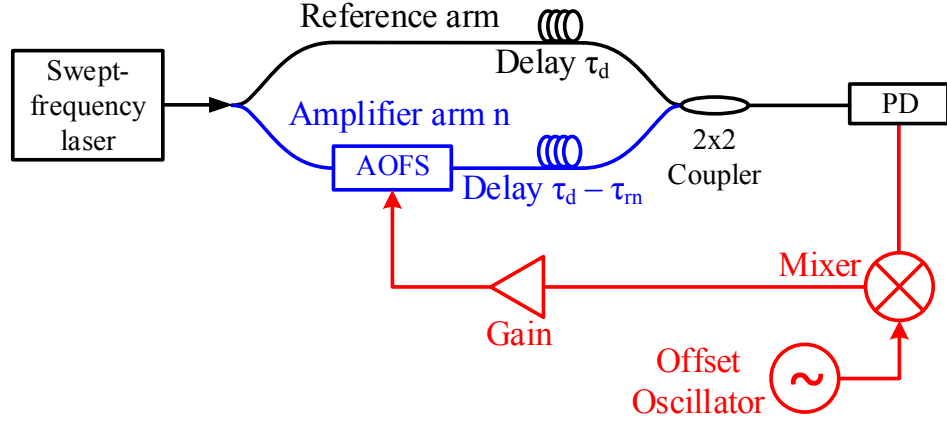
Figure 6.4: Passive-fiber chirped-wave optical phase-locked loop in the heterodyne configuration. PD: Photodetector
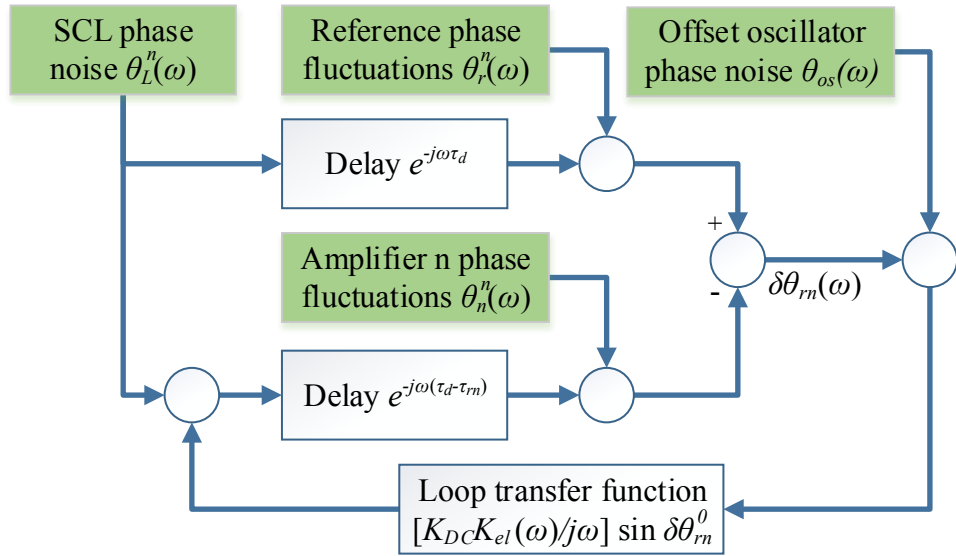

Figure 6.5: Small-signal frequency-domain model of the heterodyne chirped-wave optical phase-locked loop. The model is used to study the effect noise and fluctuations (green blocks) on the loop output variable $\delta\theta_{rn}(\omega)$.

6.3.2 Heterodyne Phase-Locking

In a heterodyne chirped-seed CBC experiment, the SFL output is split into a reference and multiple amplifier arms. The goal of the experiment is to lock the phases of all the amplifier arms to the reference, at an offset frequency ω_{os}. The heterodyne OPLL formed between the reference and the n-th amplifier is shown in figure 6.4. The bias frequency and phase shift of the AOFSs is denoted by ω_n and ϕ_n. The differential delay between the reference and amplifier arms is denoted by τ_{rn}, and we again introduce a common delay τ_d. The optical phase difference between the two arms is given by

$$
\begin{aligned}
\theta_{rn}(t) = &(-\omega_n - \xi\tau_{rn})(t - \tau_d) - (\omega_n + \omega_{L,0})\tau_{rn} - \frac{\xi\tau_{rn}^2}{2} - \phi_n \\
&- \int_0^{t+\tau_{rn}-\tau_d} K_{DC} \cos\left[\theta_{rn}(u) + \omega_{os}u + \theta_{os,n}\right] du,
\end{aligned}
\tag{6.12}
$$

where $\theta_{os,n}$ is the phase of the offset oscillator in the n-th OPLL. The steady-state solution $\theta_{rn}^0(t)$, obtained by setting the time derivative of the mixer phase $\theta_{rn}(t) + \omega_{os}t + \theta_{os}$ to 0, is given by

$$
\theta_{rn}^0(t) = -\omega_{os}t - \theta_{os,n} + \cos^{-1}\left(\frac{\Delta\omega_{fr}}{K_{DC}}\right),
\tag{6.13}
$$

where $\Delta\omega_{fr} = \omega_{os} - \omega_n - \xi\tau_{rn}$. We use this result to rewrite equation (6.12),

$$
\theta_{rn}(t) = \Delta\omega_{fr}(t + \tau_{rn} - \tau_d) + \theta_{rn}^0(t) - \int_0^{t+\tau_{rn}-\tau_d} K_{DC} \cos\left[\theta_{rn}(u) + \omega_{os}u + \theta_{os,n}\right] du.
\tag{6.14}
$$

If we acquire lock at a zero free-running frequency difference, the steady-state optical phase difference between the $n = 1$ and $n = 2$ amplifier arms is given by

$$
\theta_{12}^0 = \theta_{r2}^0(t) - \theta_{r1}^0(t) = \theta_{os,1} - \theta_{os,2} \equiv \theta_{os,12}.
\tag{6.15}
$$

The steady-state phase difference between the two amplifier arms can now be controlled electronically by setting the relative offset oscillator phase $\theta_{os,12}$. Loop oper-

ation off quadrature is therefore no longer required. The electronic phase control is also important for beam-steering and phase-controlled optical apertures.

Next, we linearize the loop about its steady-state solution. We denote the phase noise introduced in the reference and amplifier arms by $\theta_r^n(t)$ and $\theta_n^n(t)$, and offset oscillator phase noise by $\theta_{os,n}^n(t)$. We introduce $\delta\theta_{rn}(t)$, the small-signal fluctuation of $\theta_{rn}(t)$ about the steady state, so that

$$\theta_{rn}(t) = \theta_{rn}^0(t) + \delta\theta_{rn}(t). \tag{6.16}$$

We plug equation (6.16) into equation (6.14), and expand about the steady-state point (equation (6.13)). Solving for $\delta\theta_{rn}(t)$, we arrive at

$$\begin{aligned} \delta\theta_{rn}(t) = {} & \theta_{rn}^n(t) + \theta_L^n(t - \tau_d) - \theta_L^n(t + \tau_{rn} - \tau_d) \\ & - K_{DC}\sqrt{1 - \left(\frac{\Delta\omega_{fr}}{K_{DC}}\right)^2} \int_0^{t+\tau_{rn}-\tau_d} \left[\delta\theta_{rn}(u) + \theta_{os,n}^n(t)\right] du. \end{aligned} \tag{6.17}$$

When locked at quadrature, the frequency-domain description of the small-signal fluctuations is given by

$$\delta\theta_{rn}(\omega) = \theta_{rn}^n(\omega) - j\omega\tau_{rn}e^{-j\omega\tau_d}\theta_L^n(\omega) - K(\omega)\left[\delta\theta_{rn}(\omega) + \theta_{os,n}^n(\omega)\right], \tag{6.18}$$

where

$$K(\omega) \equiv \frac{K_{DC}K_{el}(\omega)\sqrt{1 - \left(\frac{\Delta\omega_{fr}}{K_{DC}}\right)^2}}{j\omega}e^{-j\omega(\tau_d-\tau_{rn})}, \tag{6.19}$$

and we have introduced the frequency-dependent electronic gain $K_{el}(\omega)$. This small-signal model is shown schematically in figure 6.5. The solution of equation (6.18) is given by

$$\delta\theta_{rn}(\omega) = \frac{\theta_{rn}^n(\omega)}{1 + K(\omega)} - j\omega\tau_{rn}\frac{\theta_L(\omega)e^{-j\omega\tau_d}}{1 + K(\omega)} - \frac{K(\omega)\theta_{os,n}^n(\omega)}{1 + K(\omega)}. \tag{6.20}$$

As in the homodyne case, for frequencies within the loop bandwidth, the OPLL reduces the phase error due to fiber fluctuations and SFL phase noise by a factor $1 + K(\omega)$. The factor multiplying the offset phase noise term $\theta_{os,n}^n(\omega)$ goes to 1 for
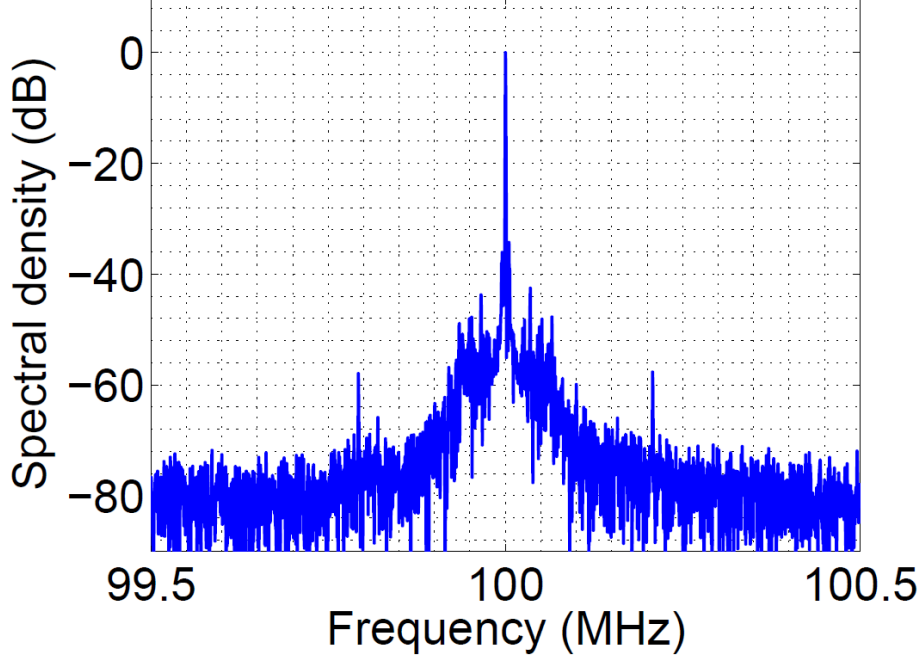
Figure 6.6: Locked-state Fourier spectrum of the measured beat signal between the reference and amplifier arms, over a 2 ms chirp interval. The nominal loop delay parameters are $\tau_d = 20$ m and $\tau_{r1} \approx 0$ m. The time-domain signal was apodized with a Hamming window.

large $K(\omega)$. The offset oscillator phase noise is transferred to the optical wave, and should be kept as small as possible.

6.3.3 Passive-Fiber Heterodyne OPLL

The heterodyne phase-locking experiment of figure 6.4 was performed at 1550 nm using a VCSEL-based optoelectronic SFL with a chirp rate of 2×10^{14} Hz/s (see chapter 3 for a summary of its operation). We used polarization-maintaining fiber-optic components, and an AOFS (Brimrose Corporation) with a nominal frequency shift of 100 MHz and a frequency modulation bandwidth of ~ 75 kHz. We used a DDS integrated circuit to provide the 100 MHz offset signal. The circuit can rapidly switch the output amplitude, phase and frequency when driven by an external trigger, which allowed us to use different locking parameters for the up and down chirps. Similarly, we designed a triggered arbitrary waveform generator in order to vary the AOFS bias during the up and down chirps. The experiment was performed for different values
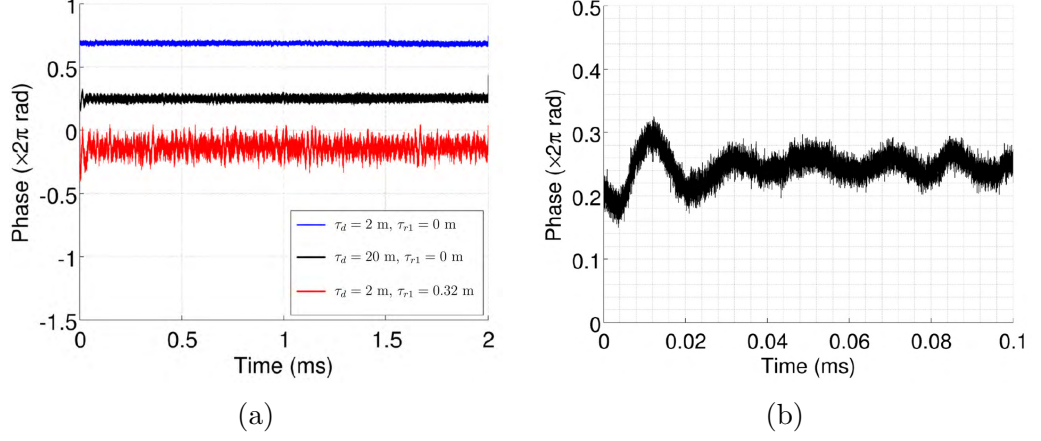
Figure 6.7: (a) Phase difference between the reference and amplifier arms calculated using the I/Q demodulation technique. The three curves (offset for clarity) correspond to different values of the loop delay τ_d and the path-length mismatch τ_{r1}. (b) Transient at the beginning of the chirp. The locking time is determined by the loop bandwidth, which is limited by the AOFS to about 60 KHz.

of the loop propagation delay τ_d and path-length mismatch τ_{r1}.[1]

We measured the beat signal between the reference and amplifier arms in order to characterize the performance of the heterodyne OPLL. The locked-state beat signal phase fluctuations, $\delta\theta_{r1}(t)$, are described in the frequency domain by equation (6.20). The variance of these phase fluctuations, $\langle\delta\theta_{r1}^2(t)\rangle_t$, is the critical metric of loop performance since it determines the fraction of the amplifier power that is coherent with the reference path [8, 104]. The spectrum of the beat signal over one 2 ms chirp duration is calculated using a Fourier transform with a Hamming window, and is shown in figure 6.6. The delay parameters were $\tau_d = 20$ m and $\tau_{r1} \approx 0$. The spectrum comprises a transform-limited peak at 100 MHz and a small noise pedestal. The loop bandwidth is about 60 kHz, limited by the AOFS. The residual noise may be calculated by integrating the noise in the spectral measurement [8, 104]. From figure 6.6, the standard deviation of the phase fluctuations is calculated to be 0.08 rad, which corresponds to 99.4% of the amplifier optical power being coherent with the reference wave.

An alternative means of analysis is to use the in-phase and quadrature (I/Q)

---

[1]The optical delay is reported here in units of length, and is to be understood as the time taken for light to propagate along that length of polarization-maintaining Panda fiber.

demodulation technique, as described in appendix A. It allows us to extract the time-domain phase fluctuations $\delta\theta_{r1}(t)$, and directly calculate the variance $\langle\delta\theta_{r1}^2(t)\rangle_t$. The locked-state phase fluctuations during one 2 ms chirp are plotted in figure 6.7a for three different values of the loop delay τ_d and the differential delay τ_{r1} (the curves are offset from each other for clarity). The locking transient is shown in figure 6.7b. The locking time is determined by the loop bandwidth, which is limited by the AOFS to about 60 KHz.

We calculated the phase error standard deviations and locking efficiencies for different delays, and the results are tabulated in table 6.1. For a given differential delay, the addition of a large loop delay $\tau_d = 20$ m slightly reduces the bandwidth of the loop, resulting in a marginally lower phase-locking efficiency. On the other hand, for a given loop delay, the addition of $\tau_{r1} = 32$ cm of differential delay results in an increased amount of SFL phase noise affecting the loop, as predicted by equation (6.20). This reduces the locking efficiency from $\sim 99\%$ to $\sim 90\%$. Differential delays much smaller than 32 cm are trivially achieved in practice, and correspond to phase-locking efficiencies larger than 90%.

Loop delay τ_d (m)	Differential delay τ_{r1} (cm)	Phase error std. dev. $\sigma_{r1} = \langle\delta\theta_{r1}^2(t)\rangle_t^{1/2}$ (mrad)	Locking efficiency $\eta = \frac{1}{1+\sigma_{r1}^2}$
2	0	47	99.8%
2	32	279	92.8%
20	0	76	99.4%
20	32	315	91.0%

Table 6.1: Measured OPLL phase error standard deviation and phase-locking efficiency for different values of the loop delay τ_d and the differential delay τ_{r1}
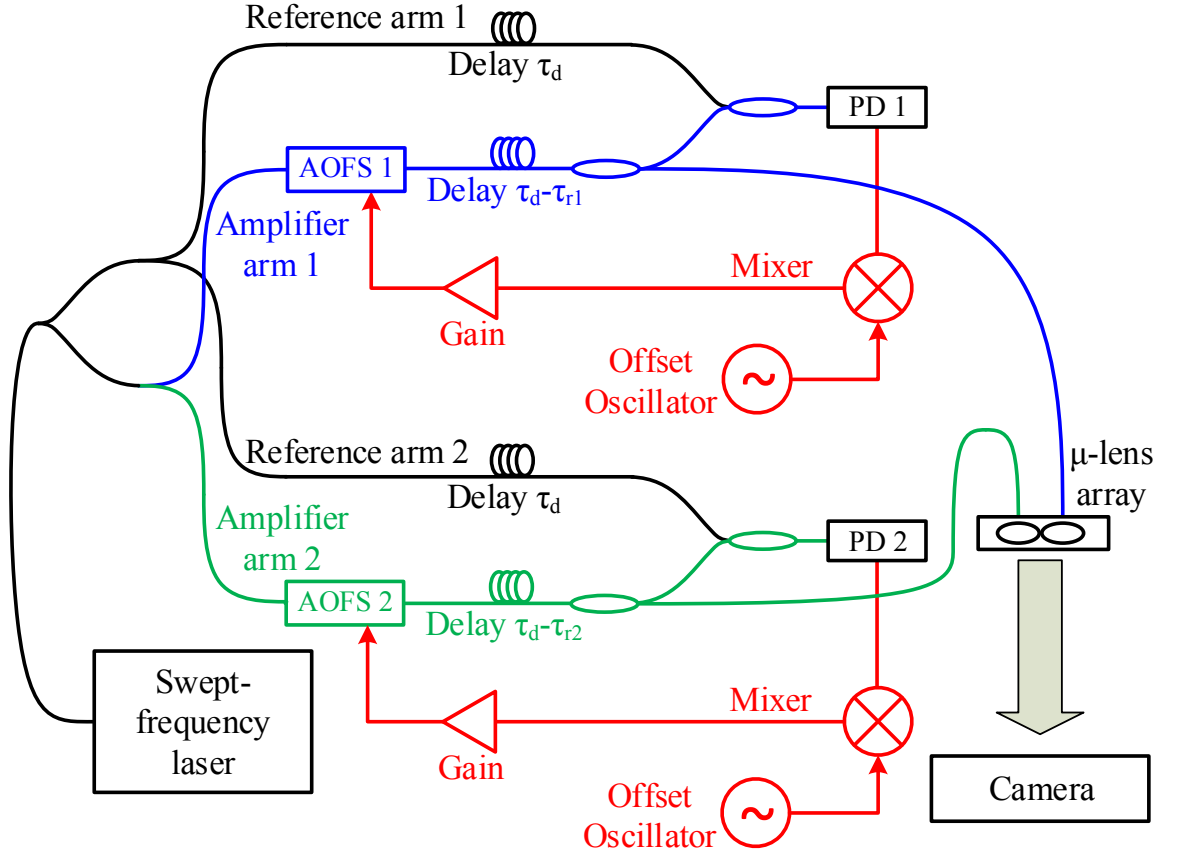
Figure 6.8: Schematic diagram of the passive-fiber chirped-seed CBC experiment with two channels. Heterodyne optical phase-locked loops are used to lock the amplifier (blue, green) and reference (black) arms. The outputs of the amplifier arms are coupled to a microlens (μ-lens) array to form a two-element tiled-aperture beam combiner. The far-field intensity distribution of the aperture is imaged on a CCD camera.

6.4 Coherent Combining of Chirped Optical Waves

6.4.1 Passive-Fiber CBC Experiment

To demonstrate beam combining and electronic beam steering, we constructed two separate heterodyne OPLLs, as shown in figure 6.8. The SFL output was split into a reference arm and two amplifier channels. The reference arm was further split into two, and delivered to the two OPLLs. The two loops were locked using electronic offset signals that were provided by a pair of synchronized DDS oscillators, with individually controllable amplitudes and phases. We measured the OPLL photocurrents in each loop for three values of the loop delay τ_d and differential delays τ_{r1} and τ_{r2}. The calculated spectra and demodulated phases are shown in figure 6.9 for $\tau_d \approx 0$ m, $\tau_{r1} = \tau_{r2} \approx 0$ cm, figure 6.10 for $\tau_d \approx 18$ m, $\tau_{r1} = \tau_{r2} \approx 0$ cm, and figure 6.11 for $\tau_d \approx 18$ m, $\tau_{r1} = \tau_{r2} \approx 32$ cm. The performance of the two loops is essentially identical. The same trend that is described above is evident in these figures—a large loop delay τ_d only slightly affects the loop bandwidth and marginally increases the measured noise levels, while the addition of a differential delay τ_{r1} or τ_{r2} increases the effect of SFL phase noise, causing a noticeable increase in the spectra pedestals and phase deviations.

The outputs of the two amplifier paths (after the AOFSs and additional fiber delays) were used to form a coherent aperture using a fiber V-groove array placed at the focal plane of a microlens array. The emitter spacing was 250 μm. A CCD camera was used to image the far-field intensity distribution of the aperture over many chirp periods. The delays in the fiber paths that deliver the amplifier channels to the microlens array are not compensated for by the OPLLs, which yields an optical frequency difference between the two channels at the aperture. We solved this issue by simply phase-locking the two loops at slightly different offset frequencies, so as to get a stable fringe pattern on the camera. Moreover, we isolated these fibers using a vibration-damping polymer sheet, in order to minimize the fluctuations in their path
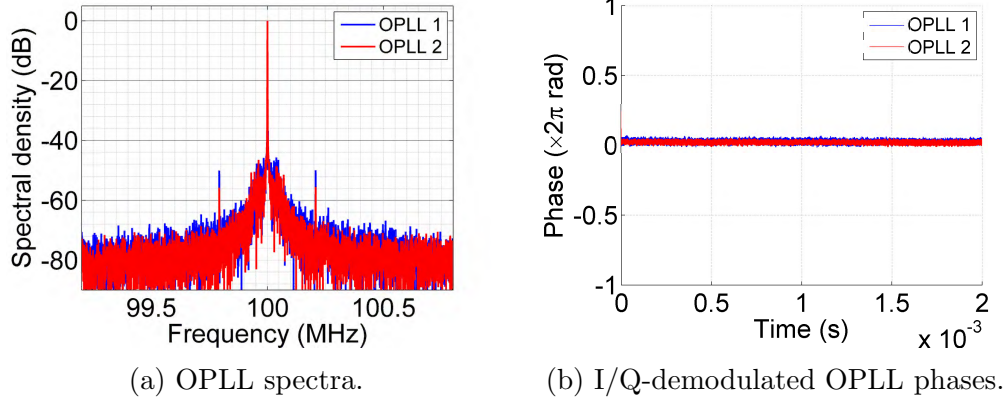
(a) OPLL spectra.

(b) I/Q-demodulated OPLL phases.

Figure 6.9: Characterization of the two heterodyne OPLLs in the locked state. $\tau_d \approx$ 0 m, $\tau_{r1} = \tau_{r2} \approx 0$ cm.
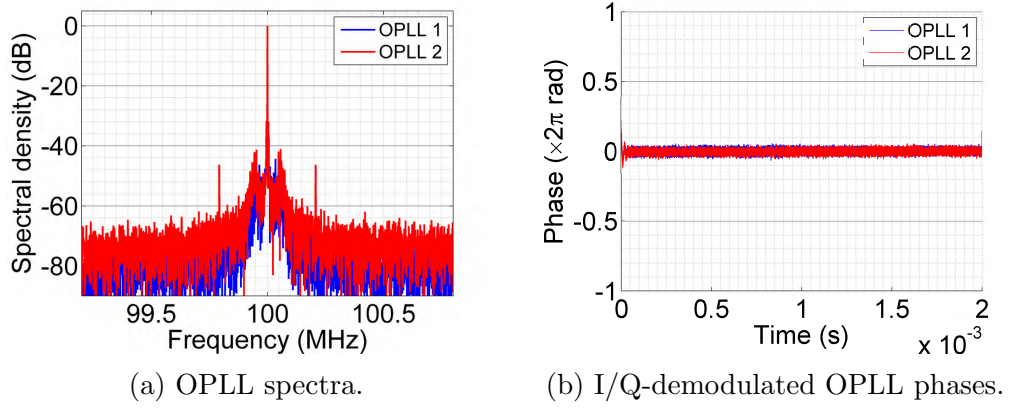

(a) OPLL spectra.

(b) I/Q-demodulated OPLL phases.

Figure 6.10: Characterization of the two heterodyne OPLLs in the locked state. $\tau_d \approx 18$ m, $\tau_{r1} = \tau_{r2} \approx 0$ cm.

(a) OPLL spectra.

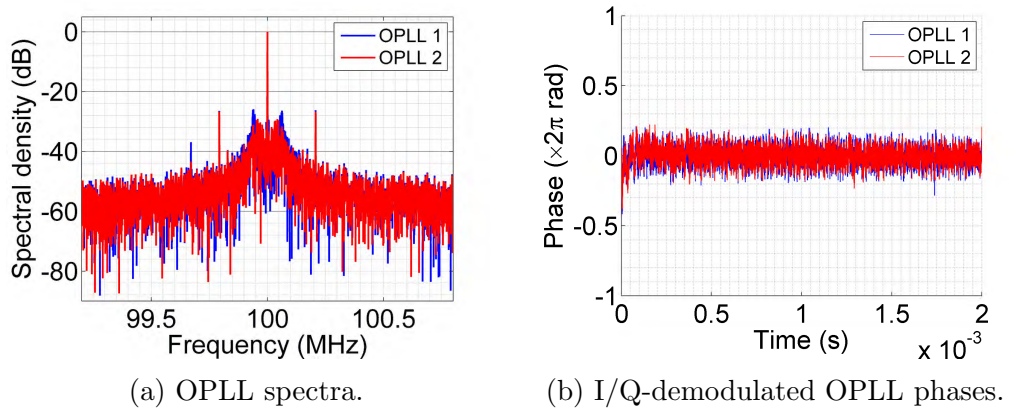(b) I/Q-demodulated OPLL phases.

Figure 6.11: Characterization of the two heterodyne OPLLs in the locked state. $\tau_d \approx 18$ m, $\tau_{r1} = \tau_{r2} \approx 32$ cm.
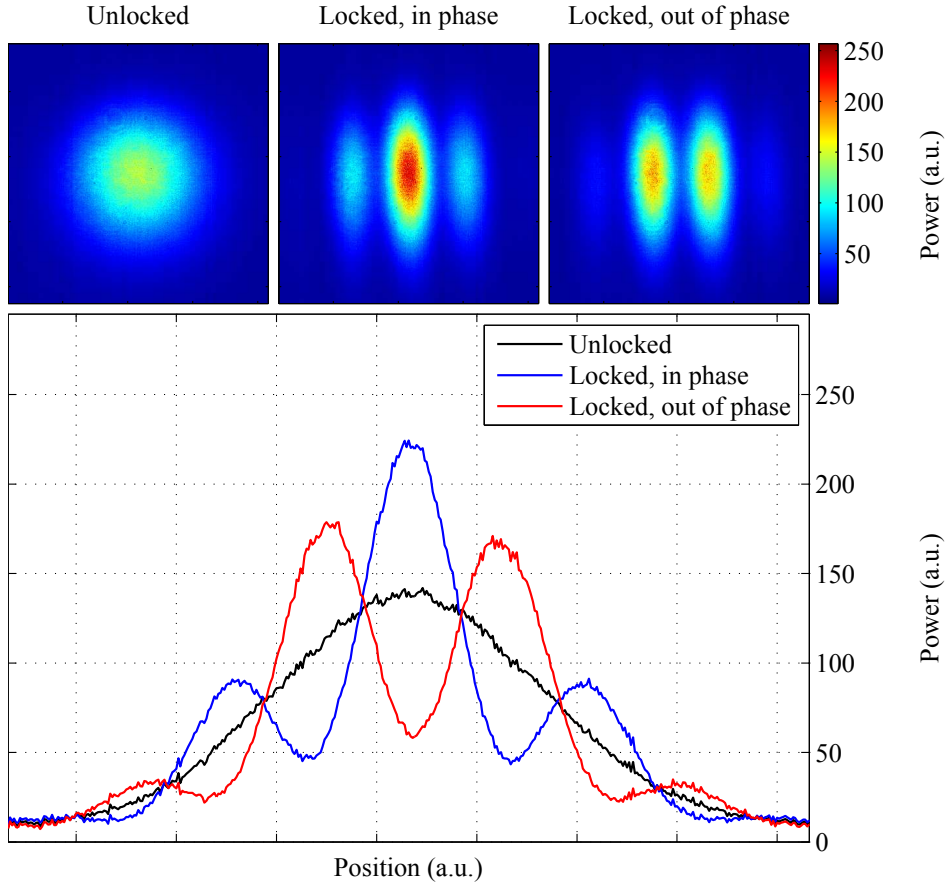
Figure 6.12: Experimental demonstration of electronic phase control and beam steering of chirped optical waves. (a) Far-field intensity profiles for the unlocked and phase-locked cases. The position of the fringes is controlled by varying the phase of the electronic oscillator in one loop. (b) Horizontal cross sections of the far-field intensity patterns

lengths. It is important to note that these efforts are not necessary in the free-space experiment of section 6.4.3

The far-field intensity distributions of the aperture in the locked and unlocked states are shown in figure 6.12. We observe a narrowing of the central lobe in the locked case vs. the unlocked case, and a corresponding increase in its intensity by a factor of 1.6. We also demonstrate electronic steering of the far-field intensity pattern by varying the phase of one of the offset oscillators, as shown in figure 6.12. The demonstrated coherent-combining approach also scales well to larger systems,

since the combination of coherent signal gain and incoherent phase errors leads to an increasing interferometric visibility with increasing number of array elements [105].

6.4.2 Combining Phase Error in a Heterodyne Combining Experiment

We briefly revisit the small-signal residual phase error analysis. So far we have focused on measuring phase errors between the reference and amplifier arms, which is useful in characterizing the OPLL performance. However, in a dual-channel combining experiment, the relevant phase error is the combining error $\delta\theta_{12}(\omega)$, given by

$$\delta\theta_{12}(\omega) \equiv \delta\theta_{r2}(\omega) - \delta\theta_{r1}(\omega) \tag{6.21}$$

Plugging in equation (6.20), we arrive at

$$\delta\theta_{12}(\omega) = \frac{\theta_{12}^n(\omega)}{1 + K(\omega)} - j\omega\tau_{12}\frac{\theta_L(\omega)e^{-j\omega\tau_d}}{1 + K(\omega)}, \tag{6.22}$$

where θ_{12}^n is the relative path-length fluctuation of the two amplifier arms. In deriving equation (6.22), we have assumed equal gains in the two OPLLs, and neglected the contribution of the offset oscillator noise.

In the experiment of section 6.4.1, we learned that the amount of differential path-length mismatch essentially determines the locked-state noise levels. From equation (6.22), it is clear that the combining noise level is actually determined by $\tau_{12} = \tau_{r2} - \tau_{r1}$, the path-length mismatch between the two amplifier arms, and not by τ_{r1} or τ_{r2} alone.

6.4.3 Free-Space Beam Combining of Erbium-Doped Fiber Amplifiers

A schematic of the dual-channel chirped-seed amplifier (CSA) CBC experiment is shown in figure 6.13. An optoelectronic SFL based on a 1550 nm VCSEL is linearly
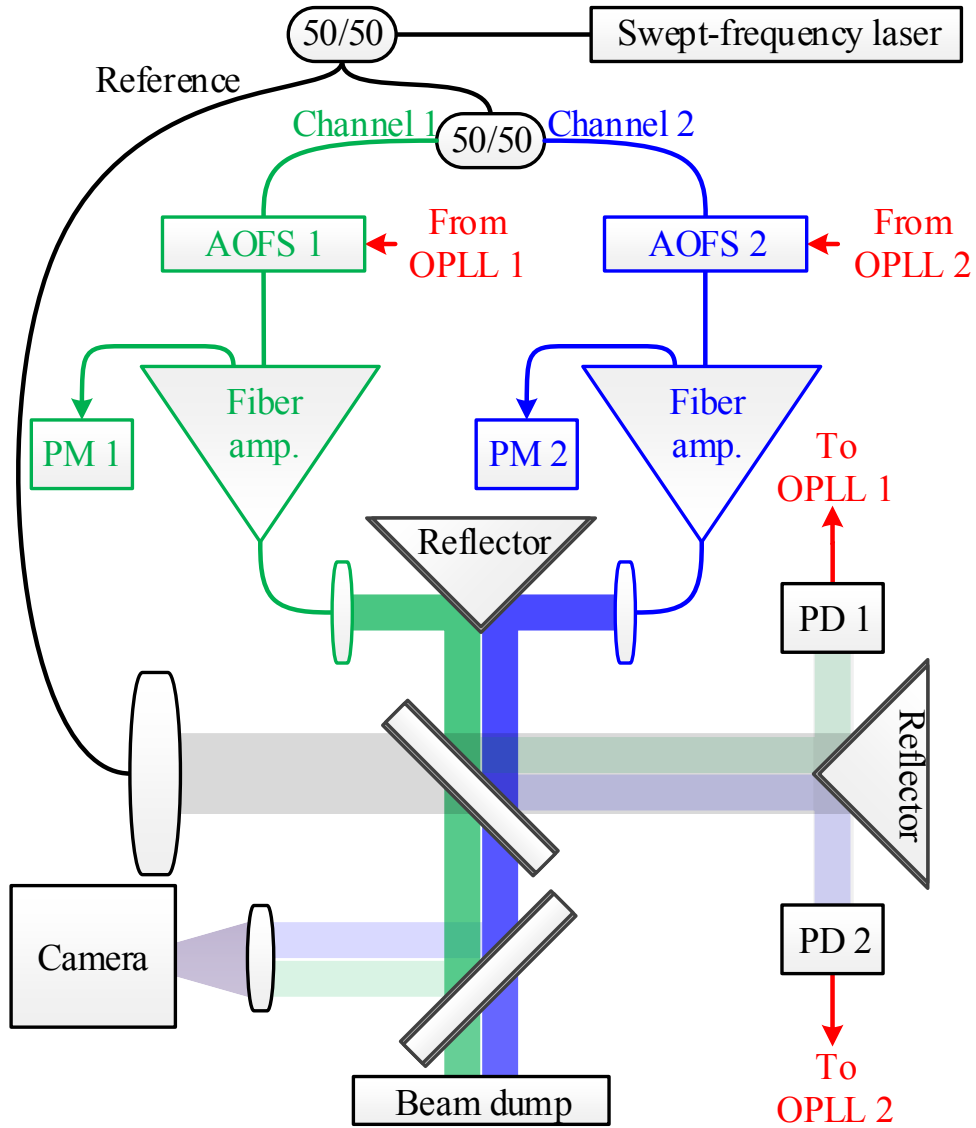
Figure 6.13: Schematic diagram of the dual-channel CSA coherent-combining experiment. PD: Photodetector, PM: Back-scattered power monitor

chirped over a bandwidth of 500 GHz in 1 ms, resulting in a sweep rate $\xi/(2\pi) =$ 5×10^{14} Hz/sec. At the end of the 1 ms sweep time, the laser is chirped in reverse at the same rate, bringing it back to its original starting frequency. Channels 1 and 2 are boosted to powers of ~ 3 W each with commercially available erbium-doped fiber amplifiers.

The back-scattered power from the 5 m final amplifier stage and the 45 m delivery fiber is recorded for each channel. We define the stimulated Brillouin scattering threshold as the power level at which the ratio of the back-scattered power to the forward power is 10^{-4}. We report a threefold increase in the SBS threshold for the 5×10^{14} Hz/sec chirp rate, when compared to a single-frequency seed.

Synchronized DDS circuits are used as offset oscillators in the two heterodyne OPLLs. An offset frequency of 100 MHz is chosen to match the nominal acousto-optic frequency shift. A tiled-aperture is formed using a 90° prism with reflecting legs, and its far-field distribution is imaged onto a phosphor-coated CCD camera with a lens.

Intensity distributions of the individual channels, as well as that of the locked aperture are shown in figure 6.14. The path lengths are nominally matched, with $l_{12} = 20$ mm. This level of path-length matching is easily achieved. We observe, in the locked state, a twofold narrowing of the central lobe and an associated increase in the peak lobe intensity. The phases of the individual emitters track the phases of the DDS oscillators, and we are therefore able to electronically steer the combined beam. Intensity distributions corresponding to relative DDS phases of $\theta_{os,12} = 0$, $\pi/2$, π, and $3\pi/2$ radians are shown in figure 6.15.

We extract the time-dependent phase differences between the reference and amplifier channels from the two photodetector signals. The phase differences corresponding to the four values of $\theta_{os,12}$ are shown figure 6.16. As expected, the OPLL phases, and hence the phases of the individual chirped waves track the DDS setpoint.

To characterize performance, we consider three path-length matching cases, summarized in Table 6.2. The I/Q technique yields the residual phase errors, $\delta\theta_{r1}(t)$ and $\delta\theta_{r2}(t)$. The time-domain combining phase error is then calculated using equation
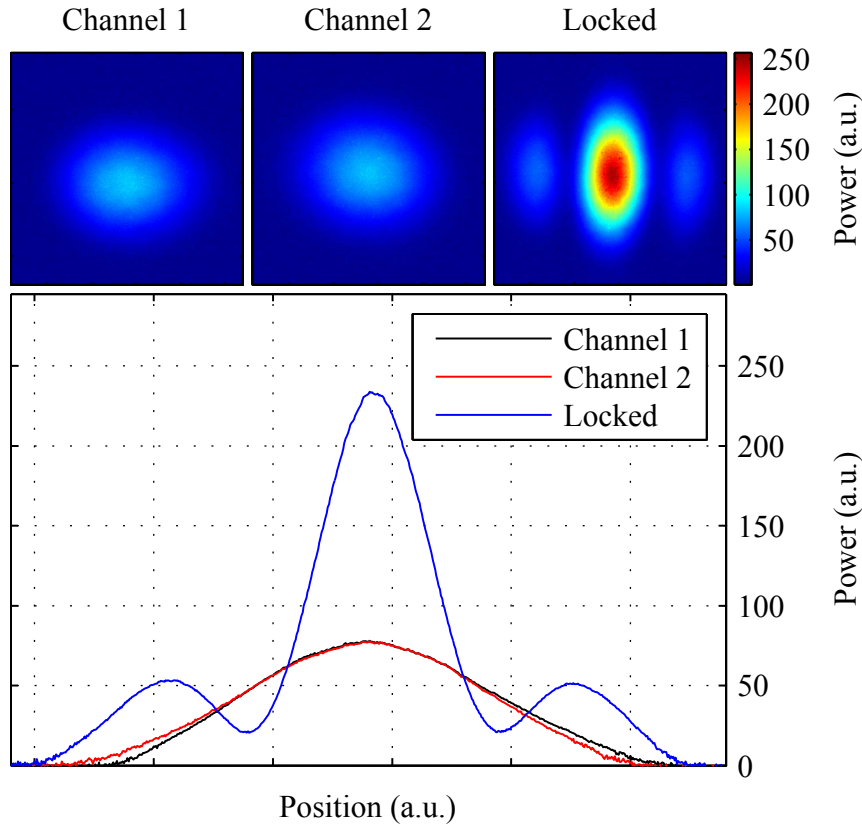
Figure 6.14: Far-field intensity distributions of the individual channels and the locked aperture. $\tau_{r1} = -19$ mm, and $\tau_{r2} = 1$ mm
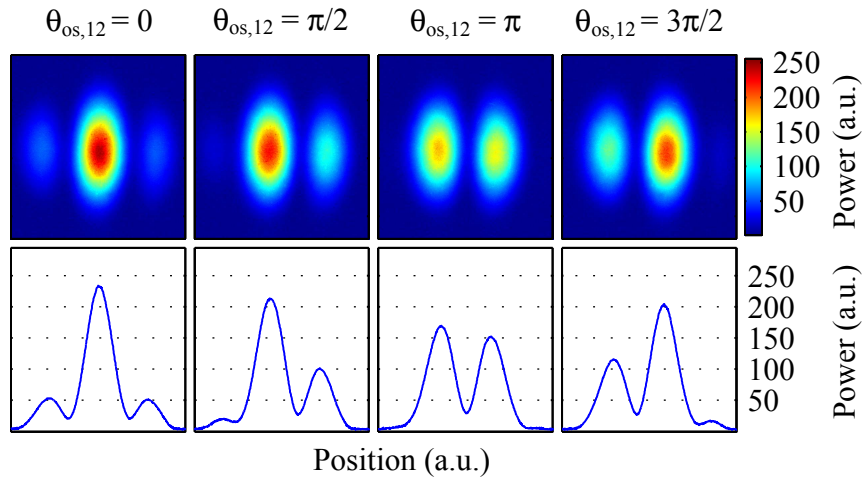

Figure 6.15: Steering of the combined beam through emitter phase control. $\theta_{os,12}$ is the relative DDS phase.
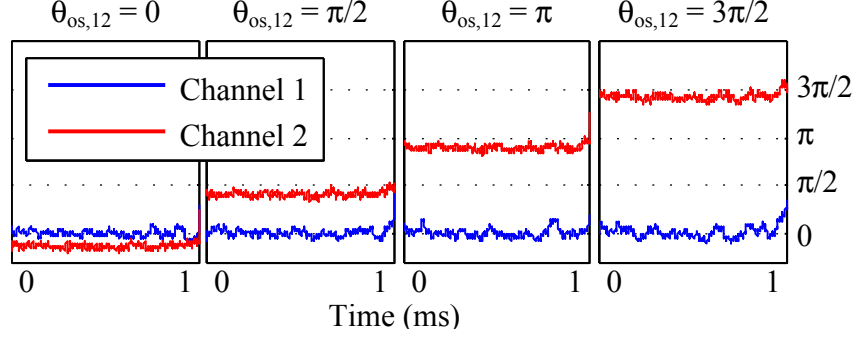
Figure 6.16: I/Q-demodulated phase differences between the amplifier channels and the reference. $\theta_{os,12}$ is the relative DDS phase.

(6.21). The standard deviations $\sigma_{xy} = \sqrt{\langle\delta\theta_{xy}^2(t)\rangle_t}$ of all three phase errors, along with the phase-noise-limited fringe visibilities are listed in table 6.2. The visibilities are calculated from the standard deviations σ_{12} using a Gaussian phase noise model, as described in appendix B.

The first case (nominally path-length-matched) has the lowest combining error, which is consistent with equation (6.22). The second and third cases have nearly identical amplifier path-length mismatches and exhibit nearly identical combining phase errors. This is consistent with the prediction that the residual combining error is determined solely by the mismatch between the amplifier channels.

The phase-noise-limited fringe visibility for the path-length-matched case is almost 99%, yet the fringe visibility in figure 6.14 is only about 80%. We believe the discrepancy is due to the wavefront distortions introduced by the collimators and the prism reflectors.

6.5 Summary

We have analyzed and experimentally demonstrated the phase-locking of chirped optical waves in a master oscillator power amplifier configuration. The precise chirp linearity of the optoelectronic SFL enables non-mechanical compensation of optical delays using acousto-optic frequency shifters, and is at the heart of our chirped phase-locking and coherent-combining systems.

We have demonstrated heterodyne phase-locking of optical waves with a chirp rate of 5×10^{14} Hz/sec at 1550 nm, achieving a loop bandwidth of 60 kHz and a phase error variance less than 0.01 rad^2. We used the heterodyne OPLL architecture to construct a dual-channel passive-fiber coherent beam combining experiment, and have demonstrated coherent combining and electronic beam steering of chirped optical waves.

We have also implemented and characterized a 1550 nm chirped-seed amplifier coherent-combining system. We used a chirp rate of 5×10^{14} Hz/sec, which resulted in a threefold increase of the amplifier SBS threshold, when compared to a single-frequency seed. We demonstrated efficient phase-locking and electronic beam steering of two 3 W erbium-doped fiber amplifier channels. We achieved temporal phase noise levels corresponding to fringe visibilities exceeding 90% at path-length mismatches of ≈ 300 mm, and exceeding 98% at a path-length mismatch of 20 mm.

The optoelectronic SFL has the potential to significantly increase the achievable output power from a single fiber amplifier by increasing its SBS threshold. Coherent beam combining techniques developed in this chapter can be used to efficiently combine multiple chirped amplifier outputs, without imposing strict path-length matching requirements, presenting a viable path towards high-power continuous-wave sources.

Case	Differential delay (mm)[a]			Phase error (mrad)			Fringe visibility
	τ_{r1}	τ_{r2}	τ_{12}	σ_{r1}	σ_{r2}	σ_{12}	$V = e^{-\sigma_{12}^2/2}$
1	-19	1	20	118	79.3	160	98.7%
2	110	450	340	184	531	428	91.3%
3	-118	220	338	150	273	410	92.0%

[a]These are fiber lengths corresponding to the time delays between the different paths. Actual mismatches have both free-space and fiber components.

Table 6.2: OPLL phase errors and phase-noise-limited fringe visibilities in the dual-channel active CBC experiment